Acoustical characterisation of a noise barrier: on a scale model, simulated and in situ

Roald Frederickx and Elisabeth Wursten
Bachelor of physics
3rd phase

May 6, 2011

Abstract

The effect of noise on man and on the environment can be quite drastic. Hence all kinds of noise barriers have been developed to reduce this problem. This paper addresses three methods to characterize the acoustical properties of such noise barriers.

First, measurements on a scale model of a simple noise barrier are described and performed. Low signal to noise ratios are taken into account, as well as the atmospherical attenuation of high frequencies.

Next, these measurements are compared to the result of a finite difference time domain simulation of that same setup. The use of a staggered grid and the correction from 2D simulation to 3D scale model are explained.

Using these measurements, reflection and refraction in the near field are briefly discussed.

Lastly, a novel method for in situ measurements is given and compared to the Adrienne method. Several flaws of the latter method are touched upon and improvements are given in situations that permit them.

1   Introduction

Noise nuisance is, unfortunately, something we encounter a lot in our day to day life. It has quite a drastic impact both on man[19] and on the environment[24].

Hence, engineers are doing the best they can to reduce this inconvenience. They design different kinds of noise reducing devices, such as the sound barriers we see next to the highway in all shapes and sizes. Our bachelor project pertains to the characterization of those noise barriers. To be more specific, to the reflection, absorption and diffraction of sound waves at such barriers.

This paper is composed of two main parts. The first part discusses two methods to characterize the acoustical properties of an object: through the use of a scale model and numerical simulation. Both will be applied on a simple model of a noise barrier and the results will be compared.

The second part deals with the acoustic characterization of life sized noise reducing devices. It contains a short description of the method we used to determine the reflection characteristics of a wall; an assessment of the standard measuring method (the Adrienne method) and a comparison of the results that both methods yielded at an in situ measurement.

2   Theoretical introduction

This section contains a short theoretical introduction to acoustics. First of all, the wave equation is derived for propagation in a fluid. Secondly, a few essential properties regarding sound reflection, absorption and diffraction are defined.

2.1   The wave equation

The derivation of the wave equation for propagation in a nonviscous fluid is based on Newton's law, the equation of continuity and the adiabatic gas law.

2.1.1 Newton's law

Consider an element of (nonviscous) fluid with mass dm in a volume $A\,dx$ (see figure 1). The force acting in the x-direction on surface A at x due to the pressure of the surrounding fluid is $F(x) = Ap(x)$, while the force at $x + dx$ is

$$F(x + dx) = -Ap(x + dx) = -A[p(x) + \frac{\partial p}{\partial x}dx].$$

Here the sign is negative since the surrounding fluid pushes the element in the $-x$-direction. The total x-component of the force on mass dm is:

$$dF_x = F(x) + F(x + dx) = A\left[p(x) - p(x) - \frac{\partial p}{\partial x}dx\right] = -A\frac{\partial p}{\partial x}dx.$$

Figure 1

According to Newton's law, this force creates an acceleration of the mass element dm:

$$dF_x = -A\frac{\partial p}{\partial x}dx = \frac{\partial v_x}{\partial t}dm = \rho_0 A\frac{\partial v_x}{\partial t}dx$$

with ρ_0 the static value of the density ρ. Simplifying the previous equation and repeating the process for the y- and z-directions yield

$$\vec{\nabla}p = -\rho_0\frac{\partial \vec{v}}{\partial t}. \tag{1}$$

2.1.2 Equation of continuity

Given that mass is conserved in fluid dynamics, we can write an equation of continuity. Consider a volume element V containing fluid. Any change of mass in V is the result of a flow of particles in or out of this volume element. A change of mass can be written as:

$$\frac{\partial m}{\partial t} = \frac{\partial}{\partial t}\int_V \rho\, dV = \int_V \frac{\partial \rho}{\partial t}dV$$

whereas the flux of particles in or out of the volume is characterised as:

$$\Phi_m = -\rho_0 \oint_A \vec{v} \cdot d\vec{A} = -\rho_0 \int_V (\vec{\nabla} \cdot \vec{v})\, dV.$$

The divergence theorem was used to obtain the last equality. Since the change of mass is equal to the mass flux, the following relation between the density and the velocity of the particles can be derived:

$$\frac{\partial \rho}{\partial t} = -\rho_0(\vec{\nabla} \cdot \vec{v}) \tag{2}$$

2.1.3 Adiabatic gas law

It is assumed that the motion of the fluid is an adiabatic process. In combination with the first law of thermodynamics this gives $\delta Q = nC_V dT + p\,dV = 0$. If we suppose the fluid to be an ideal gas, following equation holds: $p\,dV + V\,dp = nR\,dT$. Combining the previous equations gives $\gamma\frac{dV}{V} + \frac{dp}{p} = 0$ with $\gamma \equiv \frac{R+C_V}{C_V} = \frac{C_p}{C_V}$. Or in terms of the density:
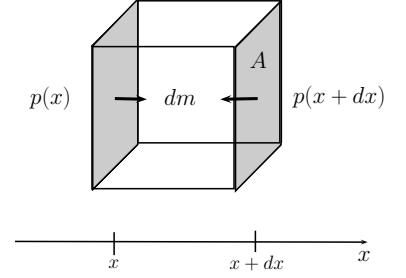
$\gamma \frac{d(m/\rho)}{m/\rho} + \frac{dp}{p} = -\gamma \frac{m}{\rho^2} \frac{d\rho}{m/\rho} + \frac{dp}{p} = -\gamma \frac{d\rho}{\rho} + \frac{dp}{p} = 0$. In the assumption that the pressure and density variations are small, the equation becomes:

$$\frac{dp}{p_0} = \gamma \frac{d\rho}{\rho_0} \tag{3}$$

with ρ_0 the static density and p_0 the mean pressure of the surroundings.

2.1.4 Combination of previous equations

Combining equations (2) and (3) gives:

$$\frac{\partial p}{\partial t} = -p_0 \gamma \left(\nabla \cdot \vec{v} \right). \tag{4}$$

Taking the time derivative of the previous equation and substituting equation (1) gives $\frac{\partial^2 p}{\partial t^2} = c^2 \Delta p$ with $c \equiv \sqrt{\frac{p_0 \gamma}{\rho_0}}$ the speed of sound in the fluid.

2.2 Some essential acoustic properties

In acoustics, several important parameters can be determined in order to characterize the acoustical properties of an object. The definitions of these parameters are stated in the following paragraphs.

2.2.1 The reflection coefficient

When a sound wave travels from one medium to another, it will be reflected and refracted at the boundary surface. Let us consider plane longitudinal waves: $p_{\text{in}} = p_{\text{in},0} exp(i(\vec{r} \cdot \vec{k}_{\text{in}} - \omega t))$, $p_{\text{ref}} = p_{\text{ref},0} exp(i(\vec{r} \cdot \vec{k}_{\text{ref}} - \omega t))$ and $p_{\text{tr}} = p_{\text{tr},0} exp(i(\vec{r} \cdot \vec{k}_{\text{tr}} - \omega t))$. Let θ_{in}, θ_{ref} and θ_{tr} be the angles respective to the normal of the surface of the incoming wave (in), reflected wave (ref) and transmitted wave (tr) respectively. The norm of the wave vectors are

$$\left\| \vec{k}_{\text{in}} \right\| = \left\| \vec{k}_{\text{ref}} \right\| = \frac{\omega}{c_1} \qquad \text{and} \qquad \left\| \vec{k}_{\text{tr}} \right\| = \frac{\omega}{c_2}$$

with c_1 and c_2 the speeds of sound in medium 1 and 2. The acoustical waves are subject to boundary conditions at the surface. First of all, the law of action and reaction dictates that the pressure should vary continuously at the boundary: $p_{\text{in}} + p_{\text{ref}} = p_{\text{tr}}$. Secondly, the normal velocity of the particles remains the same in both media at the boundary, whereas the tangential component may differ: $v_{\text{in}}^{\perp} + v_{\text{ref}}^{\perp} = v_{\text{tr}}^{\perp}$.

These boundary conditions result in Snell's law

$$\left\| \vec{k}_{\text{in}} \right\| \sin \theta_{\text{in}} = \left\| \vec{k}_{\text{ref}} \right\| \sin \theta_{\text{ref}} = \left\| \vec{k}_{\text{tr}} \right\| \sin \theta_{\text{tr}}$$

and the following solutions in terms of the pressure reflection coefficient $R_p = p_{\text{ref},0}/p_{\text{in},0}$ and the pressure transmission coefficient $T_p = p_{\text{tr},0}/p_{\text{in},0}$

$$R_p = \frac{Z_2 \cos \theta_{\text{in}} - Z_1 \cos \theta_{\text{tr}}}{Z_2 \cos \theta_{\text{in}} + Z_1 \cos \theta_{\text{tr}}} \qquad \text{and} \qquad T_p = \frac{2 Z_2 \cos \theta_{\text{in}}}{Z_2 \cos \theta_{\text{in}} + Z_1 \cos \theta_{\text{tr}}}.$$

with $Z_1 = \rho_1 c_1$ the characteristic impedance of fluid 1 and $Z_2 = \rho_2 c_2$ the impedance of medium 2. The reflection coefficient ranges from -1 to 1, while the transmission coefficient

has a value between 0 and 2. A value greater than 1 for the transmission coefficient may seem in disagreement with conservation of energy, but that is not the case. We speak of pressure coefficients, instead of intensity coefficients.

The average acoustic intensity $\vec{I}$ of a sound wave is defined as

$$\vec{I} = \frac{1}{T} \int_0^T p(t) \vec{v}(t) \, dt.$$

with p the instantaneous pressure and $\vec{v}$ the particle velocity. It equals the sound power per unit area. For plane waves, the magnitude of the intensity becomes

$$I = \frac{1}{T} \int_0^T \frac{(p(t))^2}{Z} \, dt = \frac{p_{rms}^2}{Z}.$$

The reflection and transmission coefficients are then defined as

$$R_I = \frac{I_{ref}}{I_{in}} = \frac{p_{ref,rms}^2}{Z_1} \frac{Z_1}{p_{in,rms}^2} = R_p^2 \qquad \text{and} \qquad T_I = \frac{I_{tr}}{I_{in}} = \frac{p_{tr,rms}^2}{Z_2} \frac{Z_1}{p_{in,rms}^2} = T_p^2 \frac{Z_1}{Z_2}.$$

When $Z_1 \ll Z_2$, $T_p \approx 2$, but T_I becomes 0. Hence there is no discrepancy.

2.2.2 The absorption coefficient

The sound absorption coefficient is defined as the fraction of acoustic energy that is absorbed by the surface on reflection [13, p.12]. When dealing with incident plane waves, the absorption coefficient can be written as a function of the (pressure) reflection coefficient:

$$\alpha(\theta_{in}) = 1 - |R_p(\theta_{in})|^2. \tag{5}$$

2.2.3 Diffraction

A simple rule of thumb is that diffraction effects occur when the dimensions of the obstacle are comparable to the wavelength. A more elaborate rule is given by Rindel[22] and has been applied by others[12, 1]. In the case of an infinite band of height h, it states that the diffraction in the far field can be characterized by a frequency f_0

$$f_0 = \frac{c}{\left(\frac{1}{s} + \frac{1}{r}\right) h^2 \cos^2 \theta} \tag{6}$$

with s and r the distance from the reflector to the source, respectively to the receiver, and θ the angle of incidence. For frequencies higher than f_0, there is no diffraction. For frequencies lower than f_0, the intensity is attenuated by 6dB per octave.

We will use this formula as a rule of thumb in the measurements of the scale model, even though it only applies in the far field and does not take the floor nor the width of the wall into account. More elaborate solutions that would incorporate these factors and also be valid in the near field are not analytically tractable. Hence the system will be simulated numerically in order to compare measurement with theory.

3 Scale model of a noise barrier

A scale model of a simple noise barrier is investigated. Several aspects, such as the reflection and diffraction of incident sound are examined.

4

The noise barrier

The model under consideration is composed of a wall of five wooden blocks, each with dimensions $212\,\text{mm} \times 212\,\text{mm} \times 60\,\text{mm}$. These are positioned side by side to form a barrier that is $1.06\,\text{m}$ long.

This could realistically be a 1:10 scale model of a noise barrier that is $2.12\,\text{m}$ high and $60\,\text{cm}$ wide.

The excitation source

Working with a 1:10 scale model also means that the wavelengths to be considered should be reduced by a factor of 10.

A suitable means of excitation was found in a small spark source. This produces a signal with sufficiently high frequencies and it is an excellent approximation for an ideal point source. The characteristics of the spark source are plotted in figure 2.

(a) impulse response

(b) spectrum
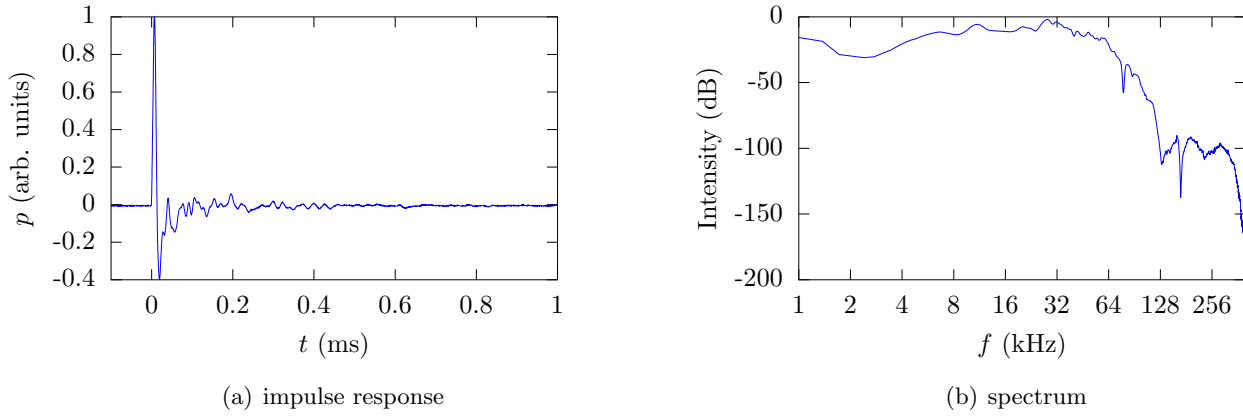
Figure 2: Characteristics of the spark source.

The spark source has a height of $15\,\text{cm}$ and was placed at a distance of $1.2\,\text{m}$ in front of the barrier for the measurements behind the wall. For the measurements in front of the barrier, the source was placed at a distance of $2\,\text{m}$.

Capturing the sound field

A programmable x-y-positioning system was used in order to scan a grid of measurement points in front of and behind the wall. The sound field at each measurement point was recorded with a high frequency microphone connected to an oscilloscope sampling at $5\,\text{MHz}$. The triggering was based on the sudden spike caused by the electromagnetic pick up of the spark on the microphone wires, this accurately defined the moment when the spark was emitted.

The scanning grid consists of 12 horizontal and 8 vertical measurement positions. The step size in each dimension is $3\,\text{cm}$ and the lowest point is at $3\,\text{cm}$ from the floor. For the measurements behind the wall, the points nearest to the wall are at a distance of $10\,\text{cm}$ from the wall. For the measurements in front of the wall, the distance between the scanned grid and the wall measured $4\,\text{cm}$.

A graphical representation of the entire setup is depicted in figure 5 on page 9.

5

Dealing with noise

Because of the very low acoustic energy associated with a single spark, additional pre-amplification was required. Even then, the signal to noise ratio was extremely low. In fact, for the lowest measurement point right behind the wall, the signal to noise ratio was of the order of one in ten!

In order to get a sufficiently clean signal at each point of the grid, each measurement was averaged over a thousand excitations. Even then, significant noise remained, especially in the measurements right behind the wall.

Figure 3 shows two averaged signals as they were received by the microphone during a measurement at a distance of 10 cm behind the wall, at both the lowest (and hence the most attenuated) and the highest (least attenuated) measurement point.

Note that the s/n ratio in the time domain plot (fig 3(a)) of the red graph is abysmal. This noise, however, seems to have a fixed pattern. A glance at the spectrum in figure 3(b) shows that this noise occurs at specific frequencies that are harmonics of 52 kHz. Due to the very high amplification of the weak signal and the low s/n ratio of a single measurement, any present noise that was in sync with the triggering became very significant in the averaged signal. The origin of this noise is possibly to be found in electromagnetic pick up from the spark generator, which charges a capacitor by pulsing it with high voltage spikes at a fixed frequency. Another possibility is that the noise originates from a part of the measurement chain, e.g. the preamplifier or the scope itself.
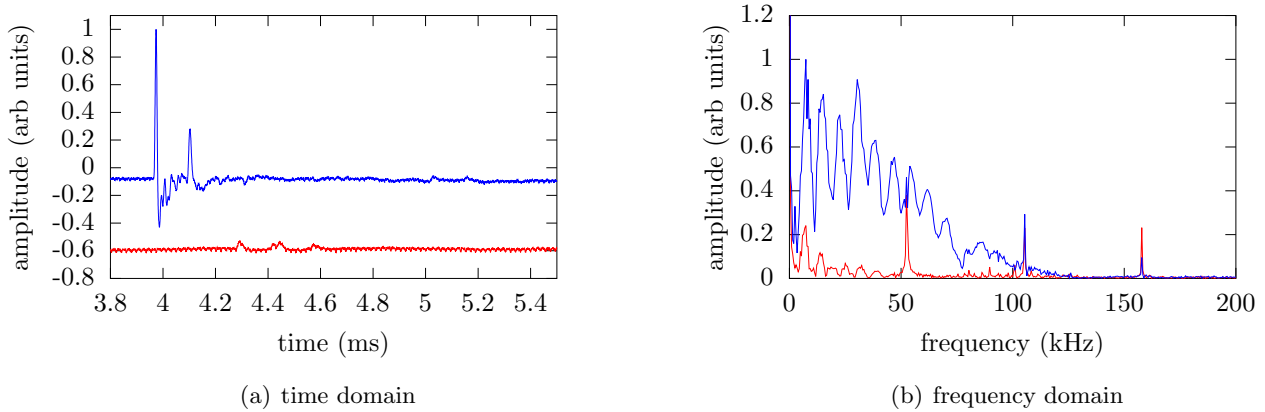

(a) time domain	(b) frequency domain

Figure 3: Raw resulting signal of 1000 averaged measurements of the scale model. The measurement was obtained closest behind the wall (10 cm distance) at the lowest (red, 3 cm high) and highest point (blue, 24 cm high, 3 cm above the wall). Notice the persistent parasitic noise at the harmonics of 52 kHz.

Averaging even more than a thousand measurements could potentially improve the s/n ratio further. However, the resulting measurement times would quickly become intractable and the noise spikes at the harmonics of 52kHz would remain nonetheless.

Apart from this high frequency noise, there were also spurious low frequency components present. All things considered, we could only get reliable spectral data in the 2 kHz to 40 kHz range, corresponding to 200 Hz to 4 kHz life sized.

Correcting for air attenuation

At the high frequencies involved in a scale model measurement, the air starts acting less and less transparent due to the excitation of the air molecules. An empirical formula that describes this effect can be found in [2] and earlier publications from the same group.

The formula we used to correct the attenuation is as per ISO 9613-1:1993, which is based on similar research. The resulting absorption for our measurement conditions is graphed in figure 4.
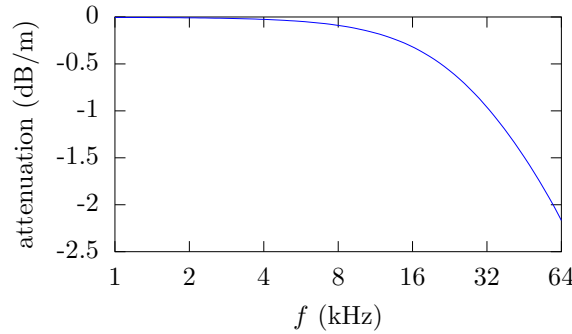

Figure 4: Atmospherical attenuation for a temperature of 18°C, a relative humidity of 60% and at a pressure of 1 atm.

The correction was implemented by using a sliding window to isolate a time slice. That slice then gets filtered appropriately to correct for the attenuation based on the mean time of that slice (and thus distance traveled). The window used was a hanning window of 400 time samples, which equals 0.08 ms. The benefit of using a hanning window is the fact that overlapping subsequent windows by half a window length preserves the energy of the signal.

Results

The results from the scale model will be discussed in depth in section 5, in tandem with the results from the simulation discussed below in section 4.

4 Numerical simulation

With the ever increasing strength of modern computers, it has become feasible to make accurate simulations of physical systems. This is often more practical than building an actual physical (scale)model. Both approaches will be compared in section 5.

4.1 Finite difference time domain method

In this section, we describe an implementation of a finite difference time domain (FDTD) method. This is a simple and intuitive way of simulating the progression of acoustic waves through a medium (in our case, air) that allows one to easily implement obstacles (eg. a hard floor, a wall). For simplicity, an infinitely long barrier on an infinitely large floor is assumed. The problem thus reduces to two dimensions.

The FDTD method consists of simulating the pressure field, p, and velocity field, $\vec{v} = (v, w)$, on a discrete spacial grid. The basic equations that govern the evolution of these fields

are equations 1 and 4, which in two dimensions read

$$\frac{\partial v(x,y,t)}{\partial t} = -\frac{1}{\rho}\frac{\partial p(x,y,t)}{\partial x}, \qquad \frac{\partial w(x,y,t)}{\partial t} = -\frac{1}{\rho}\frac{\partial p(x,y,t)}{\partial y}$$

$$\frac{\partial p(x,y,t)}{\partial t} = -\rho c^2 \left(\frac{\partial v(x,y,t)}{\partial x} + \frac{\partial w(x,y,t)}{\partial y} \right)$$

where we used $c^2 = p_0 \gamma / \rho$. These equations will be discretized in space and time. We use the shorthand notation $p_{i,j}^n$ to denote $p(x_i, y_j, t_n)$. The velocities $v_{i,j}^n$ and $w_{i,j}^n$ are defined analogously. The above equations can now be discretized as a central difference

$$\frac{v_{i,j}^{n+1} - v_{i,j}^{n-1}}{2\Delta t} = -\frac{1}{\rho}\frac{p_{i+1,j}^n - p_{i-1,j}^n}{2\Delta x}, \qquad \frac{w_{i,j}^{n+1} - w_{i,j}^{n-1}}{2\Delta t} = -\frac{1}{\rho}\frac{p_{i,j+1}^n - p_{i,j-1}^n}{2\Delta y}$$

$$\frac{p_{i,j}^{n+1} - p_{i,j}^{n-1}}{2\Delta t} = -\rho c^2 \left(\frac{v_{i+1,j}^n - v_{i-1,j}^n}{2\Delta x} + \frac{w_{i,j+1}^n - w_{i,j-1}^n}{2\Delta y} \right)$$

Here, Δt is the temporal discretization, and Δx and Δy are the spatial discretizations.

An improvement on the accuracy can be made by shifting the pressure and velocity grids by half a step in the appropriate dimensions (spacial and temporal). This is called a *staggered grid*[21], and is described by the transformation

$$v_{i,j}^n \to v_{i,j+1/2}^{n+1/2}, \qquad w_{i,j}^n \to w_{i+1/2,j}^{n+1/2}, \qquad p_{i,j}^n \to p_{i+1/2,j+1/2}^n$$

This allows one to take the central derivatives over half the previous interval, as if the discretization length has halved

$$\frac{v_{i,j+1/2}^{n+1/2} - v_{i,j+1/2}^{n-1/2}}{\Delta t} = -\frac{1}{\rho}\frac{p_{i+1/2,j+1/2}^n - p_{i-1/2,j+1/2}^n}{\Delta x}$$

$$\frac{w_{i+1/2,j}^{n+1/2} - w_{i+1/2,j}^{n-1/2}}{\Delta t} = -\frac{1}{\rho}\frac{p_{i+1/2,j+1/2}^n - p_{i+1/2,j-1/2}^n}{\Delta y}$$

$$\frac{p_{i+1/2,j+1/2}^{n+1} - p_{i+1/2,j+1/2}^n}{\Delta t} = -\rho c^2 \left(\frac{v_{i+1,j+1/2}^{n+1/2} - w_{i,j+1/2}^{n+1/2}}{\Delta x} - \frac{w_{i+1/2,j+1}^{n+1/2} - w_{i+1/2,j}^{n+1/2}}{\Delta y} \right)$$

These equations can now easily be solved for $p_{i+1/2,j+1/2}^{n+1}$, $v_{i,j+1/2}^{n+1/2}$ and $w_{i+1/2,j}^{n+1/2}$ to derive the update rules for the simulation.

Lastly, for this method to be stable, a constraint is imposed on the temporal and spacial discretization. Stability ensues only if the Courant-Friedrichs-Lewy condition is satisfied[9, 3]

$$c\Delta t \le \left[\frac{1}{(\Delta x)^2} + \frac{1}{(\Delta y)^2} \right]^{-1/2}$$

In our case, we fixed $\Delta x = \Delta y = h$ and chose Δt as the largest number to satisfy the above relation:

$$\Delta t = \frac{h}{\sqrt{2}}$$

4.2 Modelling the physical scale model

The scale model setup discussed earlier will be represented in the general framework from the previous section.

The setup of the simulation corresponds to that of the scale model discussed in section 3.

4.2.1 The grid

The setup of the grids is summarized in table 1. A visual representation of the geometry of the grids is given in figure 5.

Table 1: The setup of the grid for the finite difference time domain simulation of the scale model

Measurement	In front of wall	Behind wall
grid dimensions	$3.3\,\text{m} \times 1.4\,\text{m}$	$2.8\,\text{m} \times 1.3\,\text{m}$
spacial discretization h	$0.3\,\text{mm}$	$0.25\,\text{mm}$
temporal discretization Δt	$0.62\,\mu\text{s}$	$0.52\,\mu\text{s}$
grid size in points	11000×4667	11200×5200
position of source from left boundary	$0.75\,\text{m}$	$0.60\,\text{m}$
distance from source to wall	$2.0\,\text{m}$	$1.2\,\text{m}$

(a) measurements in front of the wall

(b) measurements behind the wall
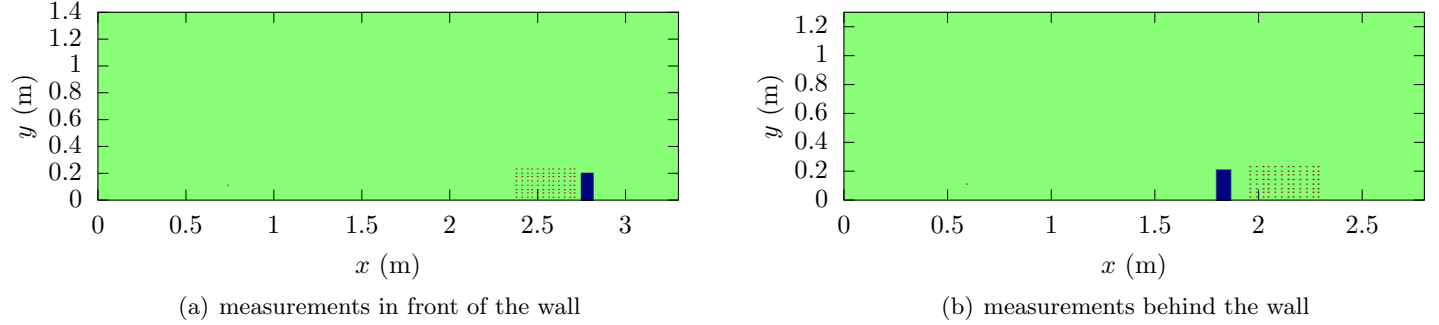
Figure 5: Visualisation of the grids used in the simulations. The mesh of points correspond to the measurement positions. The source position is indicated as a single point.

4.2.2 The excitation

The excitation signal consists of a temporal impulse shaped like a hanning function with a duration of $25\,\mu\text{s}$. This is sufficiently long to avoid temporal discretization artifacts, and sufficiently short to cover all the frequencies we are interested in. This time also approximates the duration of the actual spark used in the scale model measurements.

To avoid spatial discretization artifacts, the excitation was spread out over a two dimensional gaussian with a width 2σ of $3\,\text{mm}$. This proved to be a good trade-off between a perfect point source and excessive discretization artifacts. Note that the spark gap of the spark source used in the experiment had a comparable size of $3\,\text{mm}$.

The excitation signal is applied as a soft source[8] by simply adding it to the pressure field. Because the excitation is merely added, and not forced (as for hard sources), the actual signal that will be radiated from the source point will not be equal to the excitation signal itself. It will be altered by the response of the system. A virtual free field measurement was performed to characterize the total resulting excitation signal. The results are shown in figure 6. They can be compared to the actual spark source used in figure 2.
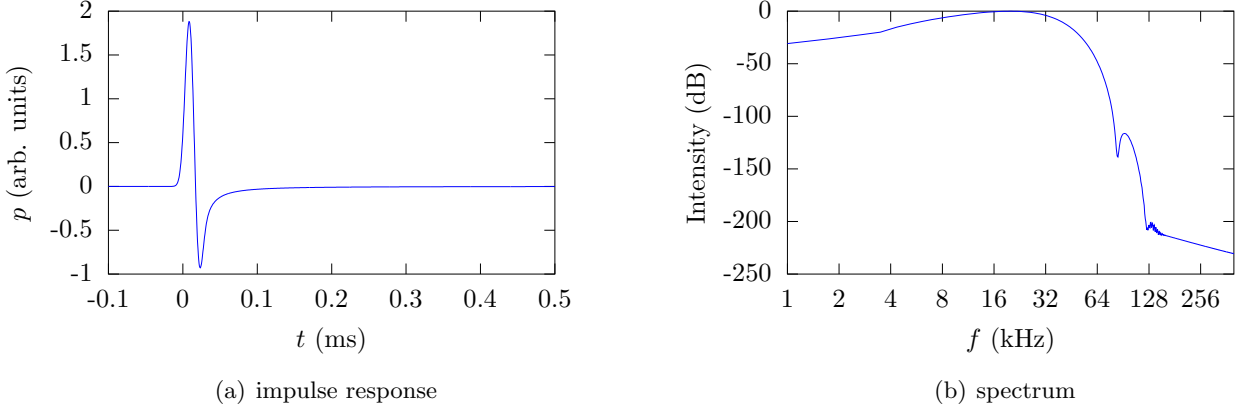
Figure 6: Characteristics of the excitation signal of the simulation.

4.2.3 The boundaries

The entire space was modelled to have perfectly reflecting edges as boundaries. The wall acting as the noise barrier was also modelled to be perfectly reflecting (ie. having an infinite impedance). This was accomplished by forcing the velocity normal to the surface to be zero. For example, for the floor this means $w_{i,0}^n = 0$ and for the left wall this means $v_{0,j}^n = 0$.

4.3 Matching 2D simulation with 3D scale model

Given the large amount of symmetry, the situation lent itself perfectly for simulation in two dimensions. However, this also means that there are some discrepancies when compared to the 3D scale model.

The most profound difference is the fact that the pressure signal of a point source in 2D (or a line source in 3D) has a $1/\sqrt{r}$ geometrical attenuation, whereas a point source in 3D has a $1/r$ dependency, with r the distance traveled. In order to be able to compare the simulation with the scale model, an extra correction of the pressure amplitudes was made to factor in the energy radiated away in the third dimension in a 3D setup.

$$p_{i,j}^{\mathrm{3D}}(t) = \frac{p_{i,j}(t)}{\sqrt{ct}}$$

Note that this correction was applied afterwards on the data of the finished the simulation, not while it was running. In every result that follows, we used the corrected pressure amplitudes $p_{i,j}^{\mathrm{3D}}$.

Additional discrepancies may occur if, for example, there are diffuse reflections on the wall in the 3D case. Those may still reach the observer and contribute to the signal, but they are not accounted for in the 2D case. However, in our case of a hard and flat wall, such effects are not expected to play a significant role.

5 Comparison of the scale model with simulation

5.1 Detailed results for several measurement positions

The results of several measurements in front of the wall are shown in figure 7. Measurements at a similar position, but behind the wall, are shown in figure 8.

Measurements in front of the barrier

For the measurements in front of the sound barrier, the direct sound that reaches the microphone is windowed out as to only keep signals that have reflected or diffracted from either the wall or the floor.

The spectra in figure 7 show a typical, broad comb structure due to the small temporal delay in the direct signal and the signal that reaches the microphone by first reflecting off of the floor. This delay increases as the distance increase, creating a comb with more 'teeth' the higher the measurement was performed.

The time domain plots of figure 7(a) and 7(b) clearly show the first strong reflections from the wall from about 6.5 ms to 6.8 ms, followed by some smaller signals that went through multiple reflections and/or diffractions.

The impulse response in figure 7(d) shows a much weaker initial signal. This is because there is no longer a direct specular reflection from the wall. The signal that reaches the microphone between 6.6 and 6.8 ms is completely ascribed to diffraction at the top of the wall. The spectrum also shows an attenuation of 20 dB per decade (whereas the previous spectra are, on average, flat). This is consistent with the rule of thumb of equation 6. It predicts a characteristic frequency f_0 of 1.8 kHz, so there should be diffraction over the entire frequency range of the plot.

Lastly, notice that the spectra and time domain signals follow the general pattern of the simulated data, though the spectra with correction for atmospherical attenuation are consistently higher than the simulated values. This is a possible result of deviating values of the temperature and humidity during the measurements, as these took about 12 hours and were done overnight. Hence the correction may have been too strong. The uncorrected spectra did not exceed those of the simulation.

Measurements behind the barrier

Figure 8 shows some results of the measurement setup where the measurements were made behind the wall. Here, the corrected spectra match the simulated spectra more intimately.

No time windowing was performed on these measurements, every signal that will get recorded will have passed the 'system' we are interested in, i.e. the noise barrier (and floor).

Figure 8(a) represents a low measurement, where we see two sets of peaks one at 4.3 and 4.5 ms and a second set at 4.6 and 4.8 ms. Each set is the result of the diffraction over the top of the wall of (1) the direct sound of the source to the top of the wall, and (2) the diffraction of the sound that reached the top of the wall by first reflecting at the floor. The second set of peaks are a diffracted signal that first reflected of off the floor before reaching the microphone. Measurements that were made on higher positions from the floor have these two sets of peaks further apart.
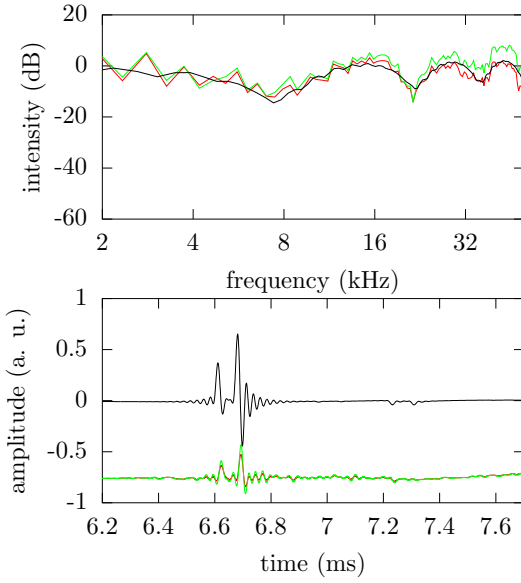
The high frequency regime of the spectrum in figure 8(a) shows an attenuation of 20 dB per decade. This is consistent with the rule of thumb of equation 6, which predicts a characteristic frequency f_0 of 1.8 kHz.
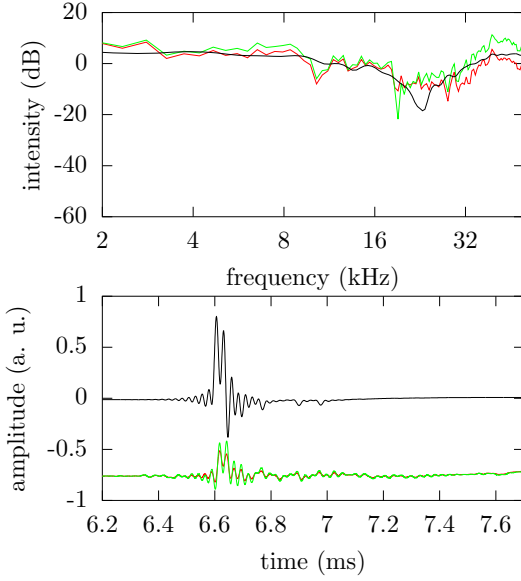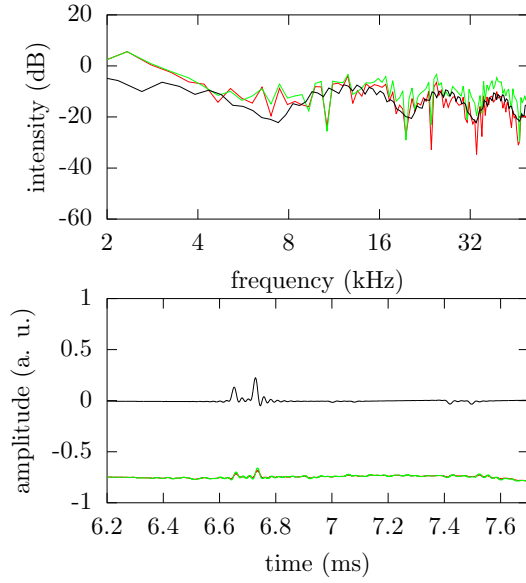
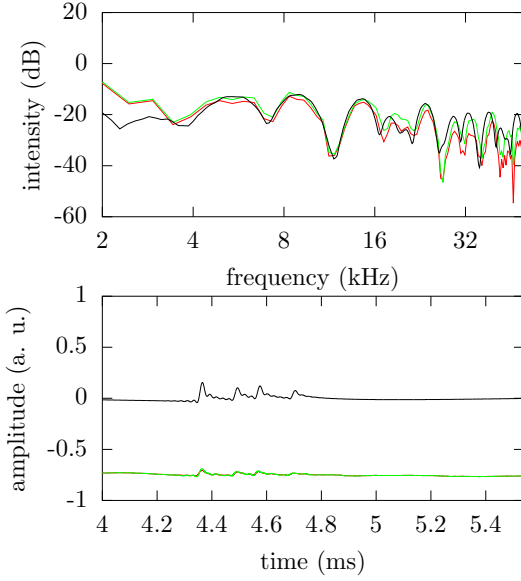(a) $x = 28\,\text{cm}$, $y = 6\,\text{cm}$
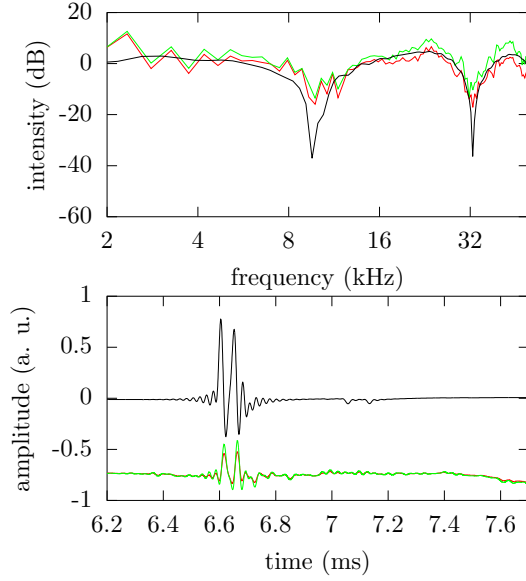
(b) $x = 28\,\text{cm}$, $y = 12\,\text{cm}$

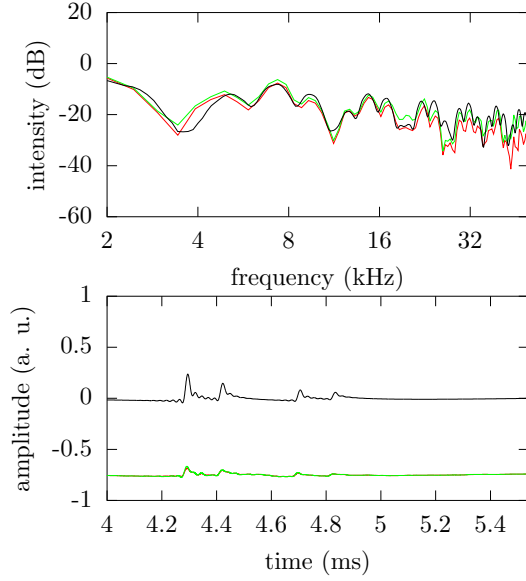(c) $x = 28\,\text{cm}$, $y = 18\,\text{cm}$
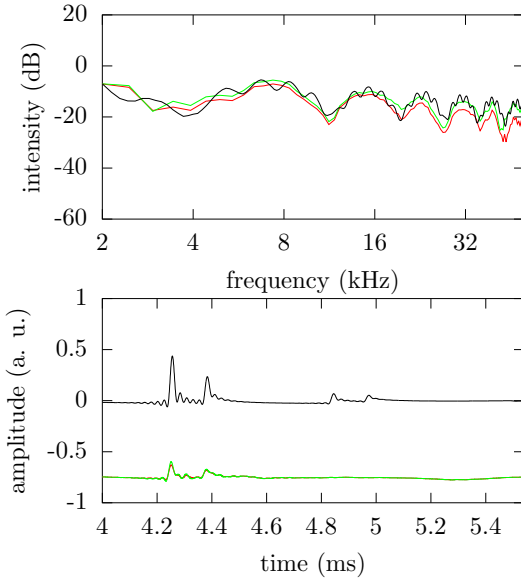
(d) $x = 28\,\text{cm}$, $y = 24\,\text{cm}$

Figure 7: Results of a selection of measurements $28\,\text{cm}$ in front of the wall, at different heights. The curves plotted are the raw measurement without (red) and with (green) correction for the attenuation of high frequencies, and the result of the simulation (black).
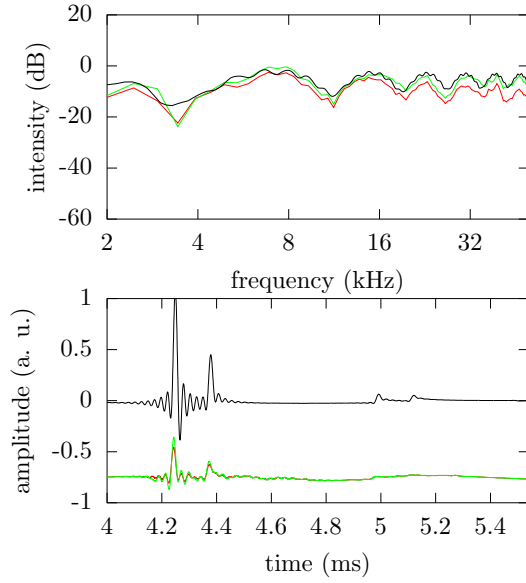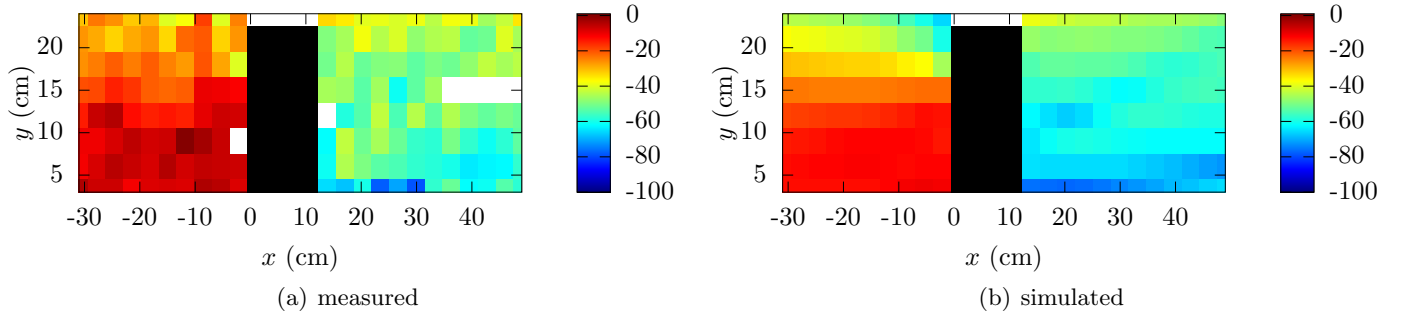
(a) $x = 28\,\mathrm{cm}$, $y = 6\,\mathrm{cm}$

(b) $x = 28\,\mathrm{cm}$, $y = 12\,\mathrm{cm}$

(c) $x = 28\,\mathrm{cm}$, $y = 18\,\mathrm{cm}$

(d) $x = 28\,\mathrm{cm}$, $y = 24\,\mathrm{cm}$

Figure 8: Results of a selection of measurements $28\,\mathrm{cm}$ behind the wall, at different heights. The curves plotted are the raw measurement without (red) and with (green) correction for the attenuation of high frequencies, and the result of the simulation (black).

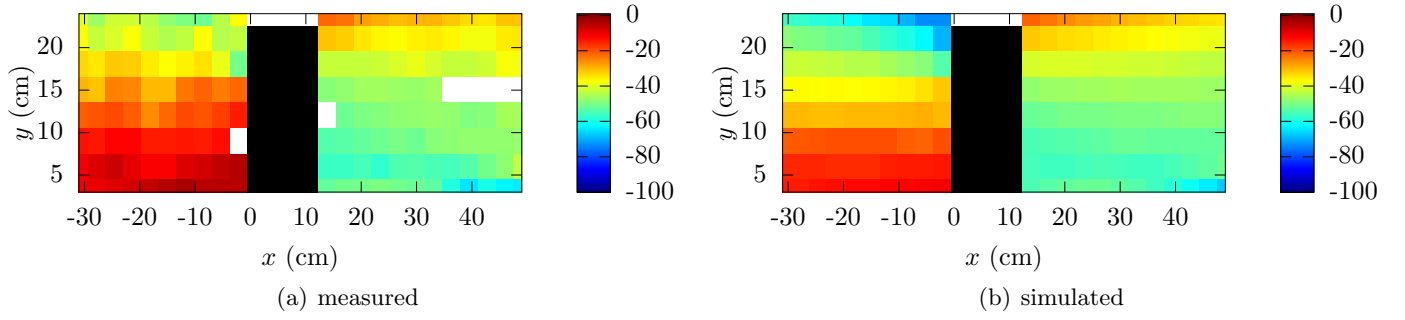**Figure 9:** Intensity (dB) in the 2.5 kHz to 5 kHz octave band.

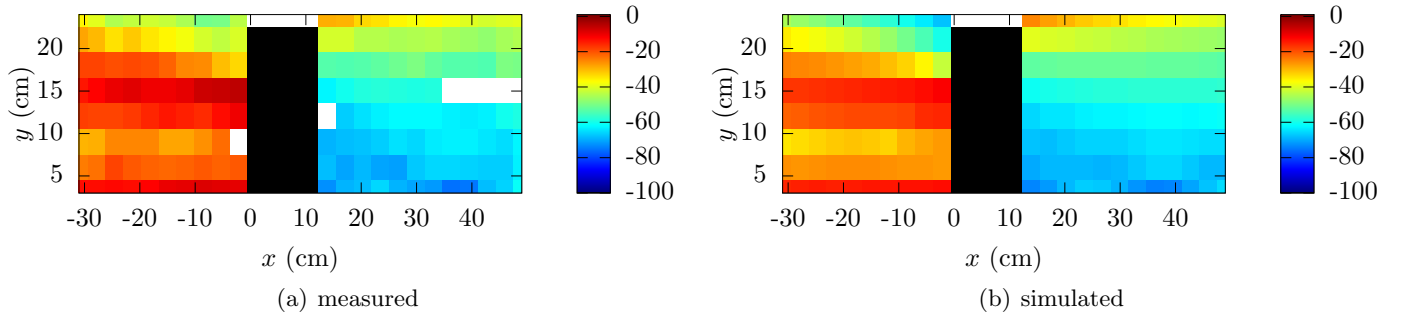**Figure 10:** Intensity (dB) in the 5 kHz to 10 kHz octave band.

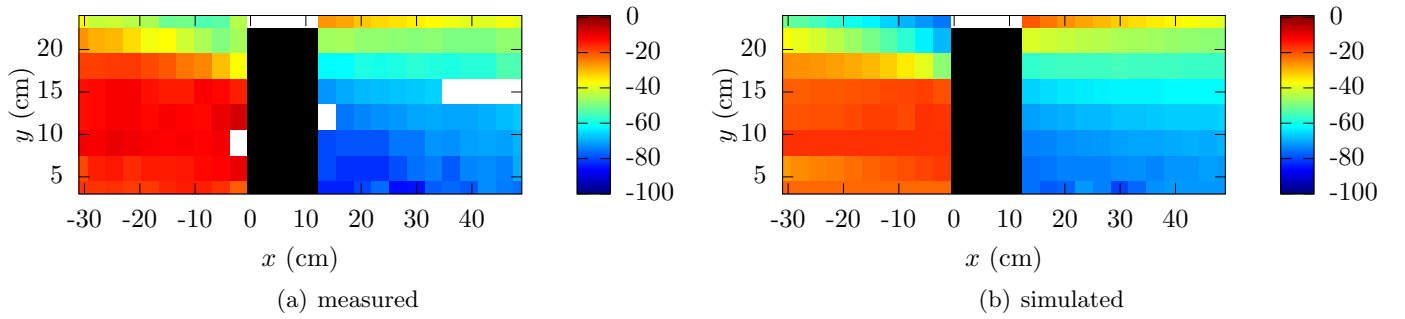**Figure 11:** Intensity (dB) in the 10 kHz to 20 kHz octave band.

Figure 12: Intensity (dB) in the 20 kHz to 40 kHz octave band.

14

This attenuation due to diffraction can also be found in figures 8(b) and 8(c), though in a lesser degree. In figure 8(d), there is a direct path from source to microphone, and this vastly overpowers the small diffraction peaks that are still present (where the diffracted signal reflected of off the floor on the side of the microphone).

5.2 Global overview of the sound field around the wall

Figures 9, 10, 11 and 12 give a visual representation of the characteristics of the wall on various spatial coordinates. Each figure represents the intensities in a fixed octave band. All intensities are normalized to the maximum of all considered octave bands so they can be compared.

The white areas in the experimental graphs represent lacking data (due to a technical error during the measurement). Also note that the frequency range in figure 9(a) is bordering on the frequency range where measurement noise becomes significant, hence the rather large deviation from the simulated graph in figure 9(b)

The comb-like shape of the spectrum also prevents from assigning a representative value to the average intensity in the small (absolute, linear) frequency span of those lower octave bands. This, by itself, also explains the noisy appearance of figure 9(a), even in the simulated part.

Diffraction becomes apparent when comparing 12(a) with 11(a) and 10(a). Lowering the frequencies by an octave raises the intensities found behind the wall (by approximately 6 dB).

6 In situ measurements of the reflection coefficient

One of the objectives of our project was to develop a suite of scripts in Matlab to record and process several acoustic signals to determine the sound characteristics of a wall. This section contains a description of our method; an assessment of the standard measuring method (the Adrienne method) and the results of an in situ measurement comparing both methods.

6.1 Recording method

The particulars regarding the measurement equipment will be discussed in the following section; as well as the methods of data gathering and processing. Furthermore, a short description of possible excitation signals will be given. Lastly, the developed method will be put to the test by measuring the absorption characteristics of a Helmholtz resonator.

Figure 13: Definition of angles θ and ϕ.

6.1.1 Recording equipment

The signal was sent from an Roland Octa-Capture sound card via a B&K amplifyer (type 2716) to the Zircon loudspeaker. The signal was captured by a B&K condensor microphone and preamplifier and sent back to the Octa-Capture sound card.

The software necessary to play and record sounds with these instruments was written in Matlab using the Data Acquisition Toolbox. The subsequent processing of these signals also took place in Matlab. The general content of this software will be discussed in section 6.1.2. But in order to do accurate measurements, the specifics of the speaker have to be examined.
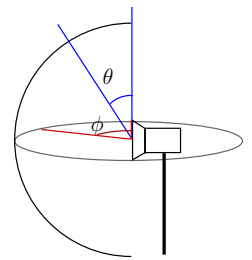
The impulse and frequency response of the Zircon speaker are shown in figure 14. The impulse response is rather short (less than 4 ms) and the frequency response has a smooth magnitude. To determine these responses, the measurement was performed in front of the speaker. However, the speaker is not omnidirectional; figures 15 and 16 show the frequency response at different vertical and horizontal angles. The definition of the angles is given in figure 13.
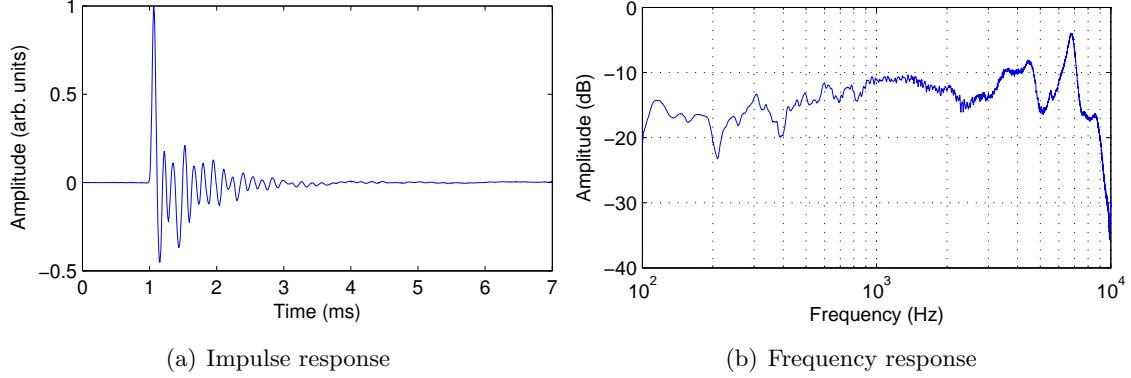

(a) Impulse response   (b) Frequency response

Figure 14: Impulse response and magnitude of the frequency response of the Zircon loudspeaker. The measurement was done in front of the speaker.

It is clear that the speaker is very directional; when doing measurements, one should keep this in mind. For θ and ϕ between 75° and 105°, the frequency response is approximately constant (per frequency). Thus, when the measured sound is reflected within that solid angle, the received signal of the speaker can be considered the same for those reflecting surfaces.

6.1.2 Data processing

The content of our Matlab program will be briefly discussed in the following paragraphs.

6.1.3 Recording

The program is capable of sending a signal to the loudspeaker while simultaneously recording the 8 analog inputs of the Octa-Capture sound card at a sample rate of 96 kHz. Due to software limitations, however, the signals can not be recorded perfectly simultaneously. A (variable) delay of the order of tens of milliseconds is possible. Hence a marker pulse should be added at the beginning of the excitation in order to facilitate synchronization later on.

There are 2 modes of recording: the first one averages n successive measurements on the spot. The excitation signal is sent to the speaker and the resulting sound is recorded. The obtained signal is then synchronized with the previous recordings by determining the peak in the cross-correlation of both signals and shifting accordingly. An additional step will be carried out to synchronize on a sub-sample time scale by means of fourier interpolation and minimizing the RMS value of the difference vector. The signal is subsequently added to the average and the cycle continues. This method gives small files, but is rather time-consuming because the signals have to be synchronized.

The second method consists of repeating the excitation signal n times back-to-back in a single recording. The averaging has to be done separately and hence the poor measurements can be filtered out of the average. The disadvantage of this method is that the files become
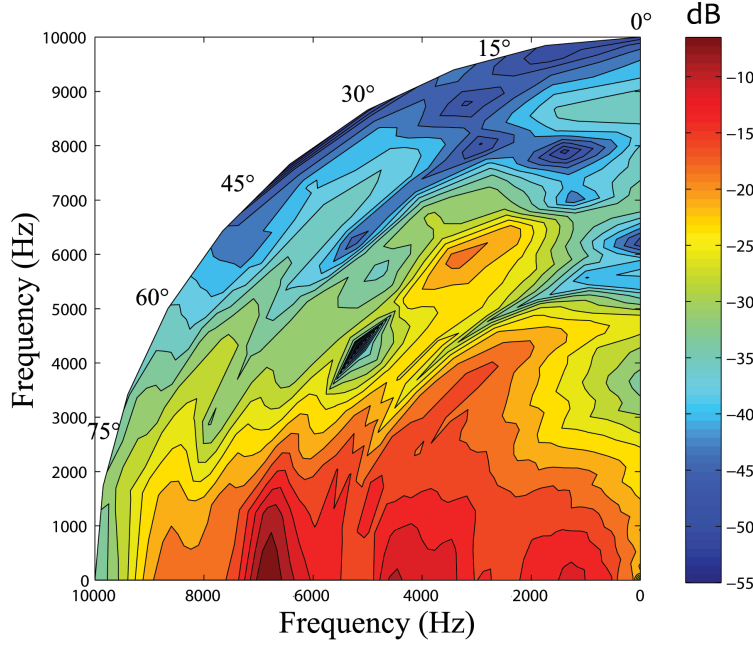
Figure 15: Frequency response of the Zircon loudspeaker for different vertical angles. The radial coordinate represents the frequency, the angle corresponds to the value of theta on figure 13. The colour gives the magnitude of the spectrum in dB.
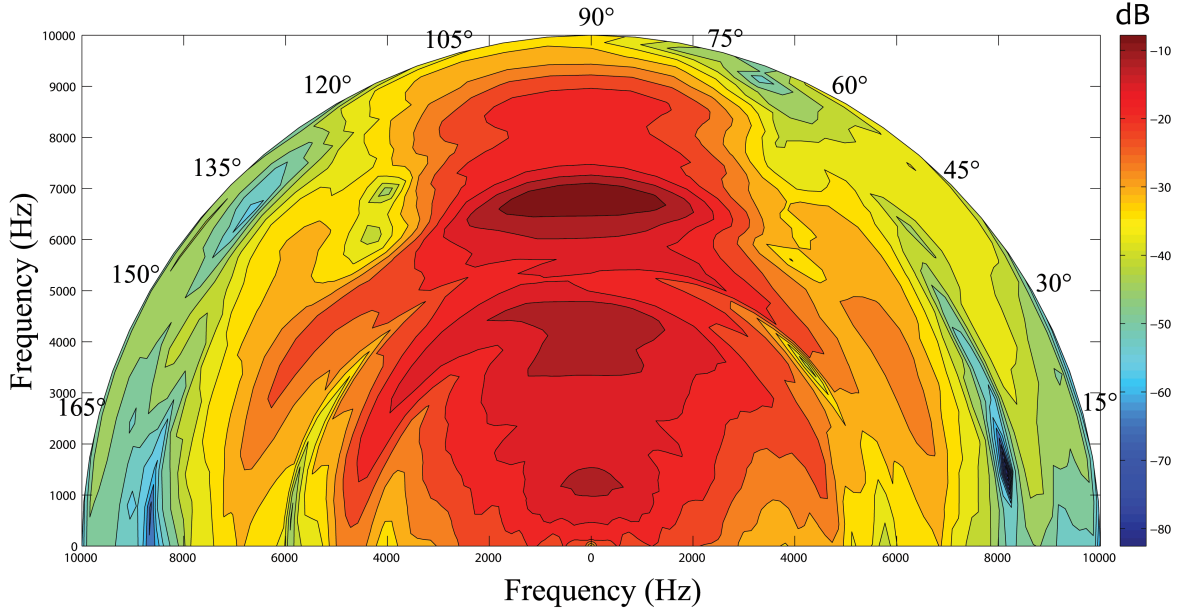

Figure 16: Frequency response of the Zircon loudspeaker for different horizontal angles. The radial coordinate represents the frequency, the angle corresponds to the value of phi on figure 13. The colour gives the magnitude of the spectrum in dB.

rather large (100 MB for 64 sweeps of 1 second), but this is compensated by the fact that the measurement time is very short.

6.1.4 Impulse and frequency response

The next step in the process is the determination of the impulse and frequency responses. The method to determine the response of the system (with speaker) is dependent on the excitation signal and will be discussed in 6.1.5. In order to procure the response of the device under test, one has to remove the parasitic reflections. This can be achieved by applying an appropriate time window on the signal. The length of the window determines the lowest possible frequency for which the frequency response can be extracted from the signal. The longer the window, the better. The window which we use in our program is based on the Adrienne temporal window (see 6.2.2). The length of the window can be adjusted by changing the length of the flat portion and the trailing end, while keeping the ratio of the lengths 7/3.

To remove the direct sound from the impulse response, our program uses the subtraction method. This method requires a free field measurement of the direct sound: the direct sound is measured with the microphone and speaker in the same relative position as during the reflection measurement, but without nearby reflecting surfaces.

The impulse response with reflections is first synchronized with the free field impulse response. This synchronzation only happens on the first few miliseconds of the impulseresponses, when there are no reflections yet, both impulseresponses are still the same.

Secondly, the free field measurement is subtracted from the signal. The resulting impulse response (which contains only the reflected component) is then windowed with an Adrienne window.

Both impulse responses are corrected for attenuation due to travel distance by multiplying the impulse response with the distance traveled (ct). And finally, the frequency response of the reflecting device is determined by deconvolving the influence of the speaker out of the resulting windowed impulse response.

6.1.5 Excitation signal

In the domain of acoustics, the two most prominent types of excitation signals are the Maximum Length Sequence (MLS) and the frequency sweep. This section contains a short description of both signal types and the way to calculate the impulse response from them.

MLS A MLS is a periodic pseudo-random binary signal with a white noise spectrum [23]. A more theoretical description of the maximum length sequence can be found in [17]. In order to recover the system response, the recorded signal has to be circularly cross-correlated with the input MLS.

Any disturbing components (not correlated with the MLS) in the measured output will be phase randomized and hence appear as uniformly distributed noise along the impulse response in stead of localized peaks in the time domain[23]. This additional noise can be reduced by averaging over multiple MLS periods.

The problem with MLS is the fact that distortion artifacts (peaks) appear in the impulse response as a result of the non linearities inherent to (mainly) the loudspeaker[13]. These additional peaks in the impulse response can not be removed by averaging over multiple periods because it is correlated with the input signal.

Frequency sweep The second type of excitation signal is the frequency sweep. The excitation signal consists of a sine function with a frequency growing in time.

To obtain the impulse response of a system excited with a sweep, one has to deconvolve the original sweep from the measured signal. This is done by dividing the spectrum of the output by the spectrum of the sweep. Doing so, however, can can cause difficulties because of dividing by (near) zero.

The remedy for this problem is placing a window in the frequency domain to dampen the areas where the spectrum of the emitted signal goes to zero. The window we use in our data processing is a hyperbolic tangent window. It is defined as:

$$w(f) = \frac{1}{4} \left(1 + \tanh \frac{f - f_1}{a_1} \right) \left(1 - \tanh \frac{f - f_2}{a_2} \right)$$

with f_1 the lower and f_2 the upper frequency bounds. The parameters a_1 and a_2 determine the width of the transitions and control the steepness of the window.

The advantage of the sine sweep excitation is that the distortion artifacts due to non linear behaviour appear before the linear response (as a result of linear deconvolution) and can be removed by time windowing[13]. Moreover, the signal-to-noise ratio for the sine sweep method is larger since the impulse response has no distortion artifacts in its tail[23].

However, the presence of impulsive noise compromises the impulse response and these residual peaks will not be properly eliminated when using signal averaging techniques. Therefore it is concluded in [23] that the MLS excitation signal gives more accurate results in the presence of non white noise, whereas the sine sweep gives better results in quiet environments.

6.1.6 Helmholtz resonator

In order to check the consistency of our program, a measurement was performed to determine the (known) absorption characteristics of a Helmholtz resonator panel. The experimental setup is presented in figure 17. The Zircon loudspeaker is positioned at an angle of 30° with respect to the horizontal. This is to ensure that both the resonator panel and the microphone receive a similar signal from the speaker.

Figure 18(a) shows the results of a measurement with a MLS of order 16 as excitation signal. At the samplerate of 96 kHz, this has a length of about 0.68 s. The plot shows the average of 64 such measurements. Plotted is the impulse response of the system, the synchronized free field impulse response, the subtracted signal and the applied Adrienne temporal window. Figure 18(b) shows the spectrum of the subtracted signal deconvolved with the free field impulse

Figure 17: Experimental setup for the measurement of the characteristics of the Helmholtz resonator panel.

response. The hyperbolic tangent window seen on the same figure was used to determine the impulse response of the Helmholtz resonator panel shown in figure 19.

The frequency dependent absorption coefficient is computed using equation 5. The result of this calculation is displayed in figure 20 as the red line. The other lines represent measurements with other excitation signals: the yellow line is obtained as the average of 16 excitations with an MLS of order 18, the green one with a sweep signal of 60 seconds and the blue line as the average of 64 sweeps of 1 second. It is clear that the results of the various measurements are consistent. Moreover, the results agree more or less with the absorption coefficient determined by L. De Geetere is his PhD thesis [13, p.84].
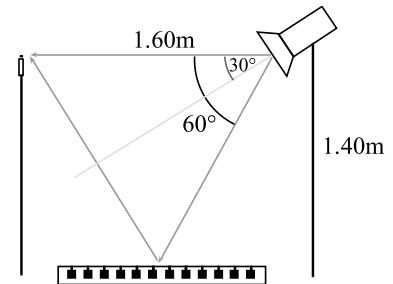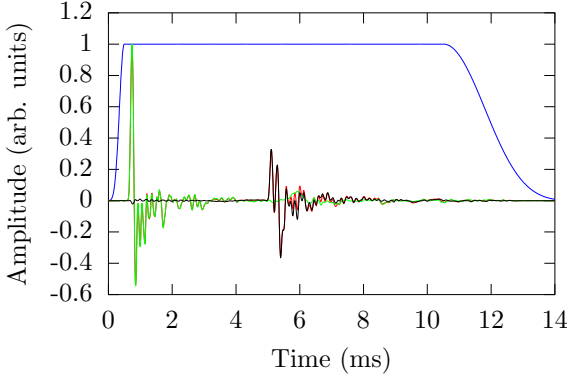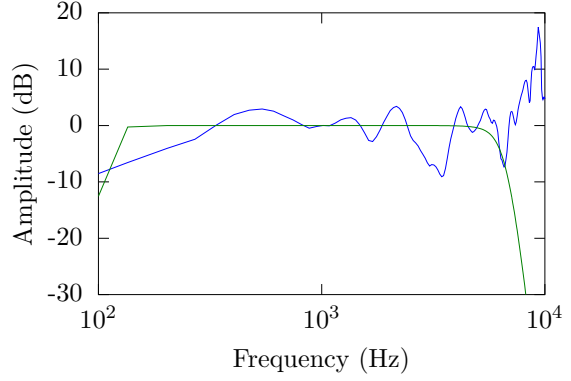
(a) Total (red), free field (green) and subtracted (black) impulse responses and the Adrienne temporal window (blue).

(b) Spectrum of the Helmholtz resonator (blue) and the hyperbolic tangent window (green).

Figure 18: Impulse responses of the measurements and frequency response of the Helmholtz resonator panel.
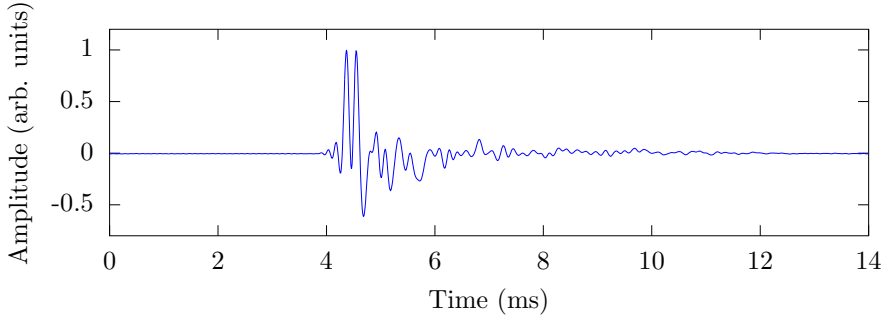

Figure 19: Impulse response of the Helmholtz resonator panel.

The main deviations are the extra peak at low frequencies (below 250 Hz) in our spectrum and the height of the peak between 6000 Hz and 7000 Hz. The appearance of the extra peak at low frequencies can be attributed to the effects of windowing in the time domain. The determination of the lowest frequencies will be compromised because of the attenuation at the beginning and tail of the signal.

A possible explanation for the peak at 6500 Hz being too high lies in the directionality of the Zircon loudspeaker. As can be seen in figure 15, the spectrum has a sudden decrease in power at frequencies around 6500 Hz and at values for θ between 45° and 60°. Since the speaker was positioned at $\theta = 120°$ in an attempt to give the direct and reflected sound the same speaker response, the angle between speaker and horizontal was *approximately* 30°. It is thus possible that due to a small deviation of the angle, the speaker responses (at 6500 Hz) were not exactly the same for both travel paths. The reflected path received less power at 6500 Hz from the speaker, which would show in the spectrum of the reflected component as a dip, or consequently as a enlarger peak in the absorption coefficient.
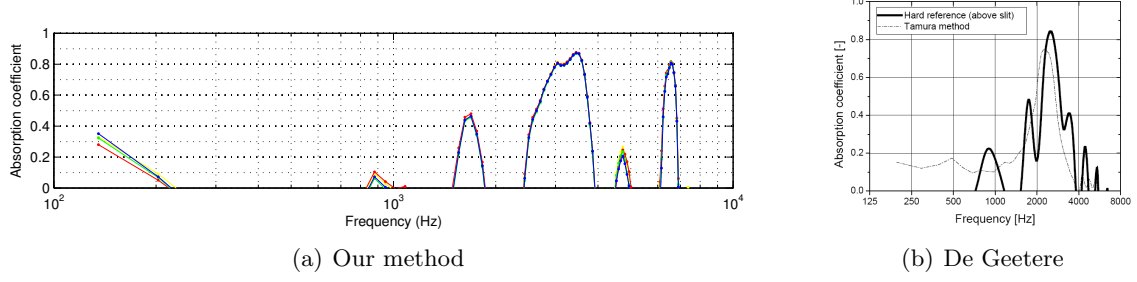
6.2 The Adrienne method

(a) Our method	(b) De Geetere

Figure 20: Absorption coefficient of the Helmholtz resonator. On the left: the results of our method with different excitation signals: 16× MLS of order 18 (yellow), 64× MLS of order 16 (red), 1× sweep of 60 s (green), 64× sweep of 1 s (blue). On the Rigth the results of De Geetere[13, p.84]

The acoustical characterisation of objects is an essential part in the design of noise reducing devices, such as the noise barriers along a motorway. It is important to be able to evaluate the performance of such barriers and more importantly to be able to compare them objectively. In order to do so a series of standardized methods was developed by CEN (European committee for standardization) to determine the performance of such devices.

One of these methods determines the sound reflection of the device and is called the Adrienne method. A short description of the Adrienne method and its shortcomings will be given in this section. For more details, see the technical specification CEN/TS 1793-5:2003 [4].

6.2.1 Experimental setup

The Adrienne method requires the setup shown in figure 21[1]. The microphone is attached to the speaker, such that the distance between them is 1.25m. The speaker is placed at a distance of 1.50 m of the wall. It is possible to swivel the speaker and microphone assembly up and down in steps of 10 degrees.

A set of nine measurement is performed with the angle varying between 50° and 130°. Several sets of measurement have to be executed at different positions and rotating along different axes dependent on the homogeneity of the sample.

The excitation signal to be used is a MLS and the signal is averaged at least 16 times.

Figure 21: Setup for the reflection index measurements according to the Adrienne method.

6.2.2 Data processing

The processing of the data happens as follows: the impulse response of a measurement is determined using cross correlation. The reflected component is extracted from the total impulse response by subtracting the direct component (obtained from a free field measurement). A time window is placed on the reflected component to remove parasitic reflections (for example from the floor).
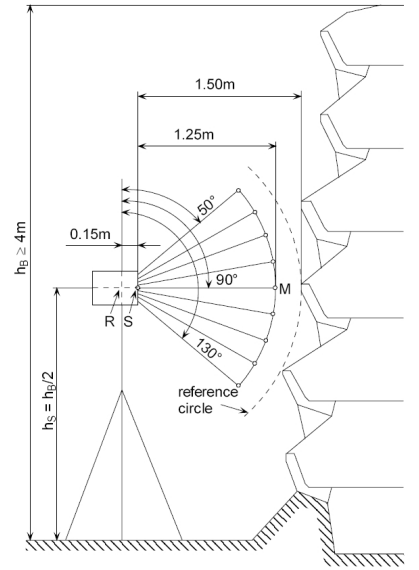
---

[1]This image was taken from [13, p.45].

The window selected for this purpose is called the Adrienne temporal window and it has the following specifications [4]:

- a leading edge of 0.5 ms with a left-half Blackman-Harris shape,
- a flat portion of length 5.18 ms,
- a trailing edge of 2.22 ms with a right-half Blackman-Harris shape.

The full Blackman-Harris window of length T is defined as

$$w(t) = 0.35875 - 0.48829 \cos\left(\frac{2\pi t}{T}\right) + 0.14128 \cos\left(\frac{4\pi t}{T}\right) - 0.01168 \cos\left(\frac{6\pi t}{T}\right).$$

This window shall be placed such that its flat portion begins 0.2 ms before the first peak of the impulse response under investigation.

With these ingredients, a parameter called the reflection index of the device under test is computed in $1/3$ octave bands using the following formula

$$RI_j = \frac{1}{n_j} \sum_{k=1}^{n_j} \frac{\int_{\Delta f_j} |\mathcal{F}\left[t \cdot h_{r,k}(t) \cdot w_r(t)\right]|^2 \, df}{\int_{\Delta f_j} |\mathcal{F}\left[t \cdot h_i(t) \cdot w_i(t)\right]|^2 \, df} \tag{7}$$

with

$h_i(t)$	the free field impulse response
$h_{r,k}(t) = h_k(t) - h_i(t)$	the reflected component of the impulse response at the k-th angle
$w_i(t)$	the Adrienne window for the free field impulse response
$w_r(t)$	the Adrienne window for the reflected component of the impulse response
$\mathcal{F}$	the symbol for Fourier transform
Δf_j	the width of the j-th one third octave frequency band
n_j	the number of angles on which to average

The parameter t which is added to both the numerator and denominator is necessary to correct for geometrical $1/r$ attenuation since $r = ct$. The reflection index is a measure for the average ratio of reflected energy and incident energy. It is this standardized quantity that is used to compare the reflection capacities of different noise barriers. For more details, see [4].

6.2.3 Shortcomings

The problem with the Adrienne method is that the directionality of the speaker is not accounted for. For example: when measuring at an angle of 130°, the path of the reflected wave will resemble figure 22. It is clear that the reflected component was emitted at a different angle than the direct component. Hence the reflected component contains a different speaker response. And this was only the case for a flat surface, imagine what would happen for non flat walls.

Another disadvantage of this setup is that the speaker itself can be the cause of the first parasitic reflection which limits the time window, since it stands relatively close to the wall. Therefore, it would be advisedly to place the speaker at a greater distance from the wall and keep the microphone close to it.

Figure 22: Path of the reflected wave.

This would not only solve the problem of parasitic reflections from the speaker, it would also reduce the influence of the speaker's directivity. The solid angle in which the response of the speaker can be considered as more or less equal remains the same, but the effective surface on the wall becomes larger. The angle between the direct sound path and the reflected sound path becomes smaller as the speaker is further removed of the wall.
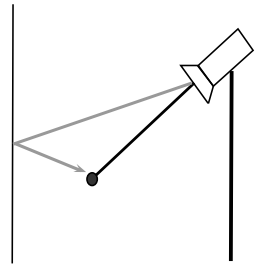
The disadvantage of placing the speaker further away, is that the ground reflection comes quicker after the reflected sound. This results in a shorter Adrienne window and consequently a larger lowest frequency limit.

Figure 23: Paths of the ground reflection and top diffraction.

The solution to this problem would be to place the speaker and microphone higher. This, however, would cause the sound wave diffracting on the top of the wall to arrive sooner. Nonetheless, when considering the fact that the diffracted wave has to travel further than the ground reflection in the Adrienne case, the height of the microphone and speaker can be adjusted so that the ground reflection and the diffracted wave arrive at the same time (see figure 23).
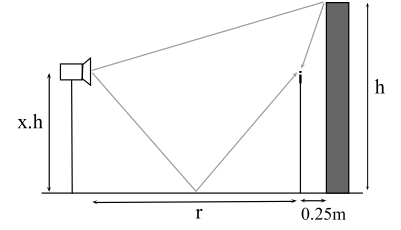
6.3   In situ measurement

In the case of a wall of 4 meters high, the speaker is positioned at a height of $2\,\mathrm{m}$ according to the Adrienne setup and the first parasitic reflection arrives $7.91\,\mathrm{ms}$ after the reflection of the wall. When placing the speaker at $2\,\mathrm{m}$ from the microphone instead of $1.25\,\mathrm{m}$, the optimal height is $2.16\,\mathrm{m}$ and the first parasitic reflection arrives $7.38\,\mathrm{ms}$ after the wall reflection. The lowest measurable frequency is $160\,\mathrm{Hz}$ for the Adrienne method and $170\,\mathrm{Hz}$ for the adapted version[2]. Since both belong to the $200\,\mathrm{Hz}$ 1/3 octave band, the loss in frequency range is minimal, but the gain in accuracy is substantial. As will be shown in section 6.3.

Figure 24: Picture of the wall and setup.

Originally, a measurement of the reflection coefficient of a noise barrier along a highway in Brussels was planned, but due to unforeseen circumstances this field trip was cancelled. As a replacement, we decided to put the Adrienne method to the test. As test subject we chose the external concrete wall of the acoustics lab at the KULeuven. The reflection index of this wall was determined with the Adrienne method by L. De Geetere [13, p.68]. His results are plotted in figure 26(b). Our goal is to ascertain the reflection coefficient of the wall while considering the directivity of the Zircon speaker and compare it with the Adrienne results (this can be done because De Geetere used the same Zircon speaker).

Our experimental setup consisted of the following: the speaker and microphone are positioned at a (maximum) height of $3.15\,\mathrm{m}$ and at a mutual distance of $3\,\mathrm{m}$. The microphone is placed at $0.25\,\mathrm{m}$ of the wall. The setup and wall are shown in figure 24. This arrangement makes sure that the first parasitic reflection arrives $10\,\mathrm{ms}$ after the wall reflection. Since the measurements are done in a noisy environment, the excitation signal is an MLS of order 16 and is averaged 64 times. To make sure that no distortion peaks occurred in the relevant time domain, a measurement was done with a sine sweep signal and subtracted. This revealed that the distortion peaks did not contaminate the important part of the impulse response.

A set of measurements was performed at horizontal angles of $90°$, $100°$, $110°$ and $120°$. This was done by keeping
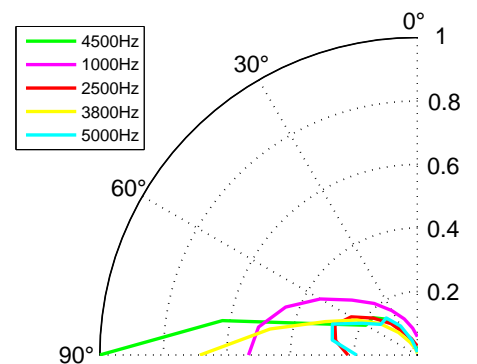

Figure 25: Angular dependence of the frequency response of the speaker for certain frequencies.

---

[2] The lowest measurable frequency is calculated as $\frac{1}{0.8T}$ with T the length of the Adrienne window [13, p.70].

the microphone at the same place and moving the speaker.
The results of this set are shown in figure 26(a). Below
400 Hz the reflection coefficient can not be considered accurate, as these spectral bands are
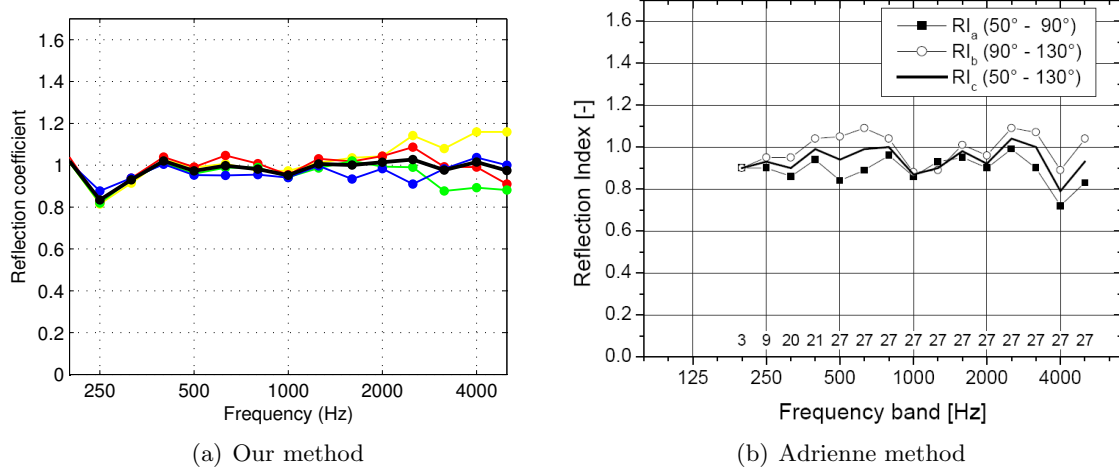only populated by a single data point.

(a) Our method

(b) Adrienne method

Figure 26: The reflection coefficient in ⅓ octave bands of the wall of the acoustics building at the KUL. On the left are the results of our measurements at 90° (yellow), 100° (red), 110° (green) and 120° (blue). The black line is the average of these 4 measurements. On the right are the results determined by L. de Geetere with the Adrienne method. The figure is taken from [13, p.68].

It is clear that there are some dissimilarities between the graphs: the Adrienne result contains dips at 1000 Hz and 4000 Hz, whereas our results remain approximately one. This discrepancy can be explained by looking at figure 15 and formula 7: the reflection index is calculated using the free field measurement as normalization for the ⅓ octave bands. For angles other than 90°, the wall receives a speaker response which differs from the free field measurement as shown in figure 22. And hence the normalization is not correct. Figure 25 shows the angular dependence of the frequency response of the speaker for several frequencies. The values at 90° correspond to the free field spectrum. For 4500 Hz, 3800 Hz and 1000 Hz, the frequency response decreases as θ deviates from 90°. Hence the calculated reflection index is an underestimate, which explains the dips in figure 26(b). For 2500 Hz and 5000 Hz, the frequency response increases as θ deviates from 90°, thus the calculated reflection index is an overestimate, which explains the increase of the reflection index at 2500Hz and 5000Hz.

7 Conclusion

In this paper, three methods to characterize the acoustical properties of a noise barrier were discussed.

First, measurements on a scale model were explored. Care was taken to correct for spurious attenuation of high frequency components due to absorption from the air. Ways of dealing with the low signal to noise ratio were briefly touched.

These measurements were then compared to a simulation of the exact same setup using a basic time domain finite difference scheme. Noteworthy was the correction to 3D of the 2D simulation and the use of a staggered grid to improve accuracy without sacrificing performance.

The measured results appeared to match with the simulation rather well, at least on a coarse level. A closer look showed some slight deviations, possibly related to atmospheric attenuation or the difference between 2D and 3D for diffuse reflections. Nonetheless, the qualitative properties were very similar in both cases. Diffraction clearly manifested itself, as could be seen in the time domain and in the frequency domain as the characteristic $6\,\mathrm{dB}$ per octave attenuation.

The third and final approach consists of measuring the acoustical performance of a life sized noise barrier. In order to do this, a program was written in Matlab to send and record sounds and to process the gathered data. The standard method for reflection measurements was assessed and it turned out that the Adrienne method does not account for the directivity of the loudspeaker.

In order to overcome this difficulty an alternative method was suggested, which involves placing the speaker higher and further away from the wall. Doing so results in a smaller frequency range, but the effect of the speaker's directivity is diminished. This improved method was used to determine the reflection coefficient of a concrete wall. The results were compared with those of the Adrienne method and it was found that the Adrienne method is subject to the directivity of the speaker, whereas the improved method gave a reflection coefficient of approximately one (as expected for a concrete wall). Although the improved method might not always be practical, it certainly is more physically correct.

References

[1] M. Barron and J. J. Bammerund. Stage acoustics in concert halls — early investigations. *Proceedings of the Institute of Acoustics*, 28, 2006.

[2] H. E. Bass, L. C. Sutherland, A. J. Zuckerwar, D. T. Blackstock, and D. M. Hester. Atmospheric absorption of sound: Further developments. *Journal of the Acoustical Society of America*, 97(1), 1995.

[3] Andreas C. Cangellaris. Numerical stability and numerical dispersion of a compact 2-D/FDTD method used for the dispersion analysys of waveguides. *IEEE Microwave and Guided Wave Letters*, 3(1), January 1993.

[4] CEN. Road traffic noise reducing devices — Test method for determining the acoustic performance — Part 5: Intrinsic characteristics — In situ values of sound reflection and airborne sound insulation. Technical Report 1793-5, CEN/TS, 2003.

[5] J. Clairbois, J. Beaumont, M. Garai, and G. Schupp. A new in-situ method for the acoustic performance of road traffic noise reducing devices.

[6] J. Clairbois and M. Garai. The new framework of en standards for traffic noise reducing devices. A-Tech / Acoustic Technologies S.A., Brussels, BELGIUM.

[7] P. Cobo, A. Fernndez, R. Palacios, C. de la Colina, and Siguero M. In situ absorption measurement of antinoise devices using pre-determined pulse waveforms. Instituto de Acstica, Madrid, 2004.

[8] Fumie Costen, Jean-Pierre Bérenger, and Anthony Brown. Comparison of FDTD hard source with FDTD soft source and accuracy assessment in debye media. *IEEE Transactions on Antennas and Propagation*, 57(7):2014–2022, 2009.

[9] R Courant, K Friedrichs, and H Lewy. On the partial difference equations of mathematical physics. *IBM Journal*, pages 215–234, March 1967.

[10] L. Cremer and H. Mller. *Principles and Applications of Room Acoustics: Volume 1.* Applied Science Publishers, London, 1982.

[11] L. Cremer and H. Mller. *Principles and Applications of Room Acoustics: Volume 2.* Applied Science Publishers, London, 1982.

[12] J. L. Davy. The directivity of the sound radiation from panels and openings. *Journal of the Acoustical Society of America*, 125(6):3795–3805, 2009.

[13] L. De Geetere. *Analysis and improvement of the experimental techniques to assess the acoustical reflection properties of boundary surfaces.* PhD thesis, Katholieke Universiteit Leuven, Leuven, 2004.

[14] William C. Elmore and Mark A. Heald. *Physics of waves.* Dover Publications, Inc., New York, 1985.

[15] M. Garai and P. Guidorzi. Experimental verification of the european methodology for testing noise barriers in situ: Airborne sound insulation. University of Bologna, Bologna.

[16] C. Glorieux and J. Wouters. *Golven en Geluid.* Katholieke Universiteit Leuven, 2011.

[17] S. W. Golomb. *Shift register sequences.* Laguna Hills, 1982.

[18] P. Guidorzi and M. Garai. Signal analysis in the sound absorption measurement procedure: The importance of time subtraction and reference surface corrections. University of Bologna, Bologna, 2008.

[19] Karl D. Kryter. *The effects of noise on man.* Orlando, Fla.: Academic Press, 2 edition, 1985.

[20] S Mller and P. Massarani. Transfer function measurement with sweeps. *Journal of the Audio Engineering Society*, 49(6):443–471, 2001.

[21] James R. Nagel. The finite-difference time-domain (FDTD) algorithm. University of Utah department of electrical and computer engineering.

[22] J. H. Rindel. Attenuation of sound reflections due to diffraction. *Proceedings of the Nordic Acoustical Meeting*, pages 257–260, August 1986. Aalborg, Denmark.

[23] G.-B. Stan, J.-J. Embrechts, and Archambeau D. Comparison of different impulse response measurement techniques. *Journal of the Audio Engineering Society*, 50(4):249–262, 2002.

[24] L. H. Watkins. *Environmental impact of roads and traffic.* London: Applied science publications, 1981.

[25] G. Watts and P. Morgan. Measurement of airborne sound insulation of timber noise barriers: Comparison of in situ method CEN/TS 1793-5 with laboratory method EN 1793-2. *Applied Acoustics*, 68:421–436, 2007.